Journal of *Marine Science and Engineering*

MDPI

Article

A Comparative Numerical Study of Hydrodynamic and Acoustic Performance Between Contracted and Loaded Tip Pump-Jet and Conventional Pump-Jet

Yu Zhao [1], Chao Wang [1], Cong Sun [1,*], Yi-Ming Hu [1], Hao-Yu Liu [1] and Min Liu [2]

[1] College of Shipbuilding Engineering, Harbin Engineering University, Harbin 150001, China
[2] China Shipbuilding Industry Corporation 719th Research Institute, Wuhan 430064, China
* Correspondence: suncong@hrbeu.edu.cn; Tel.: +86-451-82568486

Abstract

This study employs a Contracted and Loaded Tip (CLT) propeller to replace the conventional pump-jet rotor, and a comparative analysis is conducted using the Detached Eddy Simulation (DES) method. The reliability of the numerical method is first validated through open-water tests. The CLT pump-jet propulsors are systematically investigated in two series: the varying endplate width (CW) and varying endplate length (CL). The results indicate that varying the endplate width has a significant impact on the hydrodynamic performance. A smaller width leads to a more pronounced decrease in the thrust coefficient, torque coefficient, and efficiency. In contrast, varying the endplate length primarily affects the efficiency at high advance coefficients. Regarding the vortical characteristics, the gap region is dominated by the tip leakage vortex (TLV) and tip separation vortex (TSV), whose intensity and evolution are influenced by the endplate structure. A reduced endplate width expands the low-velocity region within the gap, while an increased length contributes to a more stable vortex development. In terms of the noise performance, the varying-width designs effectively suppress pressure fluctuations and achieve noise reduction. Specifically, the CW3 model exhibits maximum reductions in the overall sound source level of 5.7 dB and 4.0 dB at distances of 1 m and 20 m, respectively. Conversely, the varying-length designs intensify the pressure fluctuations and show no significant noise reduction effect.

Keywords: pump-jet propulsor (PJP); CLT; hydrodynamic performance; acoustic performance; Computational Fluid Dynamics (CFD)

Check for updates

Academic Editor: Decheng Wan

Received: 21 July 2026
Revised: 21 August 2026
Accepted: 25 August 2026
Published: 3 September 2026

Copyright: © 2026 by the authors. Licensee MDPI, Basel, Switzerland. This article is an open access article distributed under the terms and conditions of the Creative Commons Attribution (CC BY) license.

1. Introduction

The pump-jet propulsor, as a complex underwater propulsion device, has consistently been a research focus in the field of naval architecture. Studies have primarily concentrated on its hydrodynamic performance, cavitation characteristics, and acoustic performance [1–3]. With the introduction of the "Green Ship" concept, a growing number of scholars are no longer satisfied with investigating the pump-jet propulsor itself but are increasingly keen on exploring its performance optimization. In general, optimization methods are mainly divided into two categories: attaching energy-saving devices and modifying the original structure of the pump-jet propulsor. For instance, Zheng et al. investigated the addition of a Propeller Boss Cap Fin (PBCF) to a pump-jet propulsor and found that the PBCF had a positive impact on both its thrust and noise characteristics [4]. Hao et al. investigated a pump-jet propulsor with a perforated stator, and it was found that

the perforated stator trailing edge significantly reduced the vortex intensity in the region of the rotor blade leading edge (LE) and trailing edge (TE), thereby lowering the noise of the pump-jet propulsor [5]. Sang et al. equipped the rotor with an annular ring, forming a pump-jet propulsor featuring a rotor tip ring. Their research demonstrated that this configuration could effectively reduce the intensity of the tip clearance vortex and improve the internal flow field of the propulsor [6,7]. Ye et al. effectively controlled the tip leakage vortex by arranging axial grooves inside the duct of the pump-jet propulsor, which significantly increased the vortex core pressure and thereby enhanced the cavitation performance of the propulsor [8]. Xiang et al. broke away from conventional designs by updating the pump-jet rotor to a toroidal propeller. It was found that, when the toroidal propeller was applied to the Pump-Jet propulsor (PJP) of an underwater vehicle, its propulsive efficiency could reach 0.88 at an advance coefficient of 1.2 [9]. Moreover, Suryanarayana et al. [10] conducted wind tunnel experiments on a pump-jet propulsor mounted on an axisymmetric body, providing benchmark hydrodynamic performance data. Lu et al. [11] performed numerical simulations of a pump-jet propulsor and systematically analyzed its hydrodynamic characteristics, further promoting the application of CFD in pump-jet design.

The endplate structure is a simple yet highly practical device, which was first applied in the aviation field. Installing winglets at the tips of aircraft wings can effectively suppress the tip flow, thereby reducing the wing drag. Subsequently, the endplate structure was introduced into marine propellers by naval architects, leading to the development of various types of endplate-equipped propellers [12,13]. The initial research on Contracted and Loaded Tip (CLT) propellers primarily relied on potential flow methods and experimental approaches. Gaggero et al. successively investigated the performance characteristics of CLT propellers at different scales using experimental methods. Subsequently, the Boundary Element Method (BEM) was employed for the design and optimization of CLT propellers, with validation conducted via the Reynolds-Averaged Navier–Stokes (RANS) method, ultimately leading to an improvement in the CLT propeller efficiency [14]. With the rapid advancement of computer technology and Computational Fluid Dynamics (CFD), CFD methods have been increasingly employed to analyze the flow field mechanisms of CLT propellers. Notably, the tip leakage flow in rotor–duct configurations has received considerable attention. Miorini et al. [15] used the particle image velocimetry to investigate the internal structure of the tip leakage vortex in an axial waterjet pump, revealing its complex vortical topology.

Employing Large Eddy Simulation (LES), Posa investigated the tip vortices of a conventional propeller and an endplate-equipped propeller. The study confirmed a significant efficiency improvement in the CLT propeller and found that its tip vortex, while more intense, was also more stable. It was speculated that the attenuation of the tip vortex was not a direct result of installing the endplate but rather an effect of the optimized design [16]. Wang Chao et al. analyzed the instability mechanism of the tip vortex in CLT propellers using LES. The vortex trajectory was fitted, and a reliable wake vortex model was established [17,18]. Gaggero et al. investigated the wake vortex instability mechanisms in two types of CLT propellers and discovered that, depending on the endplate parameters, the instability mechanisms could undergo considerable variation [19]. Furthermore, Felli et al. [20] investigated the evolution of the propeller wake in the transition and far fields, providing fundamental insight into propeller wake instability. Gaggero et al. [21] examined the numerical prediction of the cavitating tip vortex on propellers, linking tip loading to cavitation behavior. More recently, Felli et al. [22] investigated propeller wake evolution mechanisms in oblique flow conditions, and Posa et al. [23] examined the wake structure of a propeller operating upstream of a hydrofoil, both of which further highlight the importance of tip vortex stability and its relevance to endplate-equipped propellers.

Based on the literature reviewed, the CLT structure can enhance propeller efficiency and refine the wake flow, particularly its vortical structures. This indicates that the structure holds potential for improving the acoustic performance of propulsors. However, the current research has been confined to CLT propellers themselves, with no studies yet applying the CLT structure to other types of propulsors. Therefore, this paper applies the CLT structure to a pump-jet propulsor to analyze its effects on both the hydrodynamic and acoustic performance of the pump-jet propulsor.

2. Numerical Methodology

2.1. Governing Equations

For a continuous, homogeneous, incompressible, viscous fluid, the governing equations consist of the continuity Equation (1) and the momentum Equation (2):

$$\frac{\partial \overline{u_i}}{\partial x_i} = 0 \tag{1}$$

$$\frac{\partial \overline{u_i}}{\partial t} + \overline{u_j}\frac{\partial \overline{u_i}}{\partial x_i} = \overline{f_i} - \frac{1}{\rho}\frac{\partial \overline{p}}{\partial x_i} + \nu\frac{\partial^2 \overline{u_i}}{\partial x_j \partial x_j} - \frac{\partial \overline{u_i' u_j'}}{\partial x_j} \tag{2}$$

where ρ denotes the fluid density; p denotes the pressure; ν denotes the kinematic viscosity coefficient of the fluid; $\bar{u}_i$ and u'_i represent the Reynolds-averaged velocity and the fluctuating velocity of the fluid, respectively; and f denotes the body force acting on the fluid. For the present fully submerged simulation without free surface or cavitation, the gravity term has a negligible effect on the relative hydrodynamic performance and can be equivalently absorbed into the modified pressure; it is retained here only for the completeness of the governing equation. The subscripts i and j denote the three dimensions of the coordinate system.

The turbulence model was selected based on the need to capture the unsteady vortex structures and associated pressure fluctuations, which are essential for both hydrodynamic and acoustic predictions. The pump-jet flow field involves strong tip leakage vortices, flow separation, and vortex shedding, which are difficult to capture accurately with RANS models. LES would provide higher fidelity but is computationally expensive for the present configuration. Therefore, the DES approach based on the SST k-ω model was adopted, as it combines RANS treatment in the near-wall region with LES in the separated and wake regions. This provides a good balance between computational cost and the ability to resolve the dominant unsteady flow structures that govern the acoustic sources.

The governing equations are solved using the Detached Eddy Simulation (DES) method. DES operates by employing LES in regions with strong flow separation and switching to RANS modeling within boundary layers. Consequently, it combines the advantage of lower computational cost from RANS with the higher accuracy of LES in resolving transient flows, making it a well-established approach for solving unsteady flow fields. The SST *k-ω* turbulence model is adopted as the underlying RANS model when invoked.

In the SST model, the turbulent length scale is defined as follows:

$$l_{k-\omega} = \frac{k^{1/2}}{\beta^* \omega} \tag{3}$$

where β^* is a constant, typically taken as 0.09.

Following the fundamental principle of DES, Equation (3) is redefined as follows:

$$\hat{l} = \min(l_{k-w}, C_{\mathrm{DES}}\Delta) \tag{4}$$

where C_{DES} is a specified constant and Δ is the filter scale of the sub-grid-scale model.

The above formulation enables the turbulence model to switch to a sub-grid-scale model (i.e., utilizing LES for solution) when the turbulent length scale is large, and to revert to the SST model for solution when the length scale is small. This switching mechanism is governed by the function F_{DES}.

$$C_{\mathrm{DES}} = (1 - F_1)C_{\mathrm{DES}}^{k-\varepsilon} + F_1 C_{\mathrm{DES}}^{k-\omega} \tag{5}$$

where $C_{\mathrm{DES}}^{k-\varepsilon} = 0.61$; $C_{\mathrm{DES}}^{k-\omega} = 0.78$.

By combining Equations (3)–(5), we obtain the following:

$$\varepsilon = k\beta^{*}\omega \max\left(1, \frac{l_{k-\omega}}{C_{\mathrm{DES}}\Delta}\right) = k\beta^{*}\omega F_{\mathrm{DES}} \tag{6}$$

To mitigate the stress loss arising from the switching between the RANS and LES modes within the model, Menter reformulated the blending function F_{DES} as follows:

$$F_{\mathrm{DES}} = \max\left[\frac{l_{k-\omega}}{C_{\mathrm{DES}}\Delta}(1 - F_{\mathrm{SST}}), 1\right] \tag{7}$$

Since F_{SST} in the SST model is nearly zero within the boundary layer, this formulation ensures that F_{DES} remains in RANS mode inside the boundary layer.

2.2. Geometry

The baseline pump-jet propulsor developed by our team (Table 1, Figure 1) and its derived CLT variants (Figure 2) are adopted for computation. Key variable parameters of CLT rotors are given in Table 2.

Table 1. Key parameters of the pump-jet propulsor.

Item (Unit)	Value
Rotor Diameter D_R (mm)	237.5
Number of Rotor Blades *kr*	7
Hub Diameter Ratio	0.3
Pitch Ratio at 0.7 Radius $P_{0.7}/Dr$	1.8
Gap Height (mm)	1.5
Number of Stator Blades *ks*	9

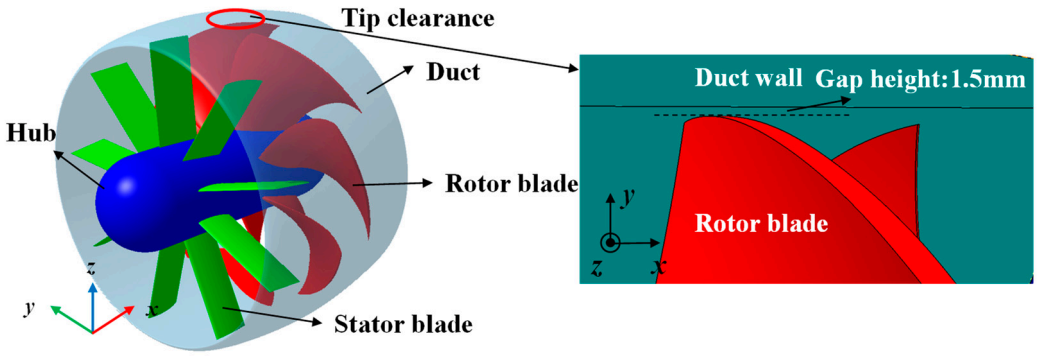


Figure 1. Pump-jet propulsor geometry.

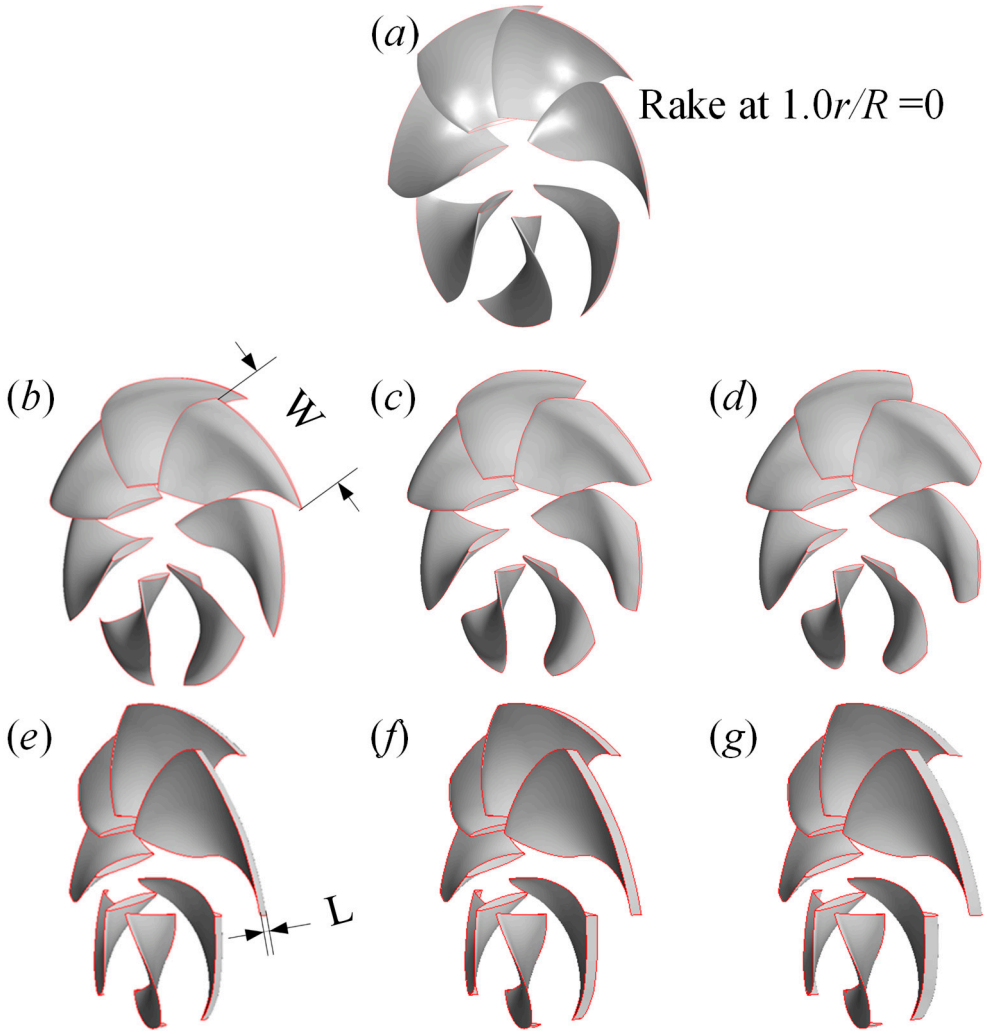


Figure 2. The six CLT-type pump-jet propulsor models: (**a**) baseline, (**b**–**d**) variable width (CW) series, and (**e**–**g**) variable length (CL) series.

Table 2. Parameter variations at the 1.0r/R profile for CLT-type rotors.

Classification	Model	Chord Length at 1.0r/R (mm)	Rake at 1.0r/R (mm)
Baseline	Proto	0.473	0
Variable Width Series	CW1	0.473	0.023
	CW2	0.423	0.023
	CW3	0.382	0.023
Variable Length Series	CL1	0.473	0.005
	CL2	0.473	0.008
	CL3	0.473	0.010

For the variable endplate width series, the longitudinal inclination (rake) of the endplates at the radial position r/R = 1.0 is consistently set to 0.023 for all three models. Their chord lengths are 1.0C_0, 0.9C_0, and 0.8C_0, respectively, corresponding to a progressive decrease in endplate width. For the variable endplate length series, in order to effectively eliminate the downstream tip vortex flow when the rotor tip cap is parallel to the inner wall of the duct, the endplate inclination angle is set to 90°. This means the endplate is perpendicular to the tip surface and parallel to the duct inner wall. The chord length at r/R = 1.0 for all three models in this series remains constant at 1.0C_0, while their longitu-

dinal inclination values are 0.005, 0.008, and 0.010, respectively, resulting in a progressive increase in endplate length.

Two families of CLT-type rotor variants are designed following a one-factor-at-a-time strategy to decouple the influences of tip chord width and tip rake inclination. For the variable width series (CW1–CW3), the tip rake value is fixed at 0.023 mm, while the tip chord length is gradually reduced. This group isolates the effect of tip chord width under constant rake offset. For the variable length series (CL1–CL3), the tip chord length remains identical to the baseline Proto model (0.473 mm), and only the tip rake magnitude is increased. This configuration isolates the hydrodynamic effect of tip rake and the associated 90-degree trailing-edge inclination, with unchanged chord geometry. The selected ranges were determined based on the baseline model dimensions and preliminary numerical evaluations, and were chosen to cover a representative variation while remaining within practical geometric and structural limits. This allows the individual influence of each parameter to be clearly identified without introducing excessive performance degradation or flow separation that would obscure the comparison.

2.3. Simulation Settings and Boundary Conditions

The numerical simulations in this study were performed using the commercial CFD software Siemens Star-CCM+ (V2206), which is based on the finite volume method. The solver employs a second-order upwind scheme for spatial discretization of the convective terms and a second-order implicit scheme for temporal discretization. The pressure-velocity coupling is handled using the SIMPLEC algorithm. These numerical schemes are consistently applied across all simulations to ensure numerical stability and accuracy.

The entire computational domain is divided into a stationary domain and a rotating domain. The rotating domain encompasses the rotor and the rotor-section hub, while the stationary domain contains the remaining pump-jet components (stationary parts) and the flow field region. The overall computational domain is constructed as a cylinder with a radius of $5D_R$ and a length of $15D_R$, with the rotating domain positioned $5D_R$ from the inlet. The inflow surface is set as a velocity inlet, the outflow surface as a pressure outlet, and all other boundaries are defined as slip walls. The interface between the two domains is configured as an interface to facilitate data exchange. The specific division of the computational domain is illustrated in Figure 3. The computational domain extends $5D_R$ upstream and $10D_R$ downstream of the test section. A $5D_R$ inlet offset was adopted to provide sufficient flow development length and to match the experimental inlet measurement location. The $10D_R$ downstream extent was selected to avoid outlet boundary effects on the region of interest. Similar domain configurations have been validated and widely adopted in relevant pump-jet numerical studies in published literature [24].

To ensure consistency with the open-water tests, the inlet velocity was set equal to the carriage speed for each operating point, and the outlet static pressure corresponded to the hydrostatic pressure at the model immersion depth. The inlet turbulence intensity was specified as a typical low value for towing tank conditions, and its effect on the predicted forces was found to be negligible. The fluid density and viscosity were taken from the measured water temperature during the tests. The computational geometry was identical to the experimental model. The rotor rotational speed was fixed at n = 16 rps, matching the experimental value.

Figure 4 illustrates the computational grid used in this study. To capture the details of the rotor wake vortical flow field, refinement was applied to the tip vortex region. The boundary layer on the duct and stator was configured with 10 layers, while the rotor boundary layer was set with 15 layers, with the first layer having a thickness of 10^{-5} m. The DES computations in Star-CCM+ adopt the built-in full-wall y+ treatment. The area-

averaged wall y+ on all pump-jet solid surfaces remains below 6 across the computational domain (Figure 5).

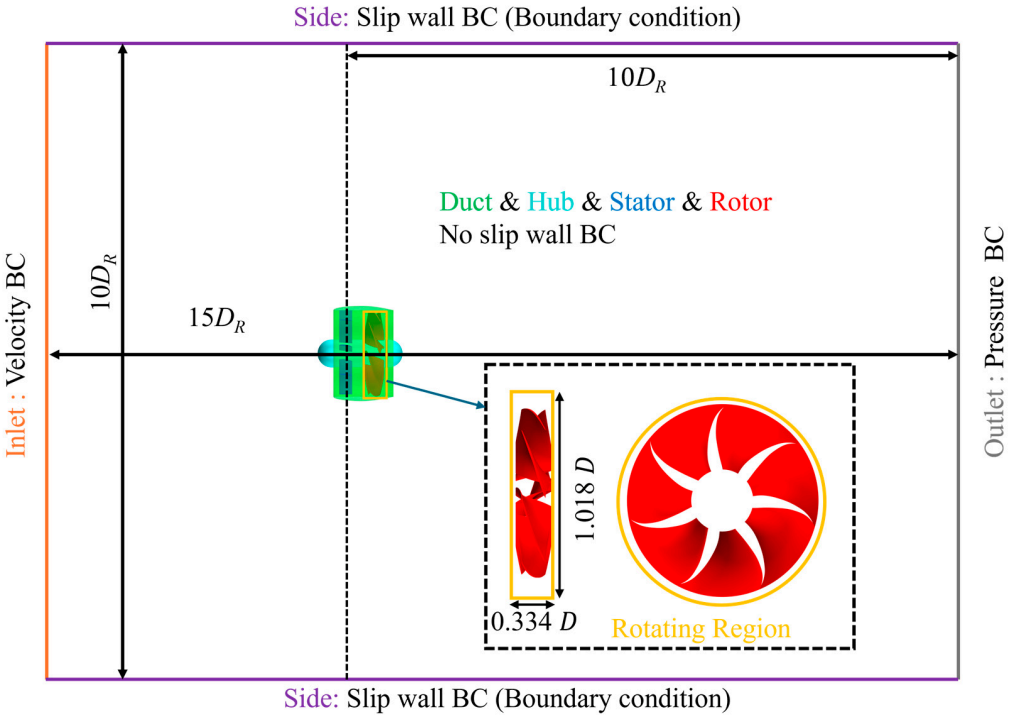


Figure 3. Computational domain and boundary condition setup.

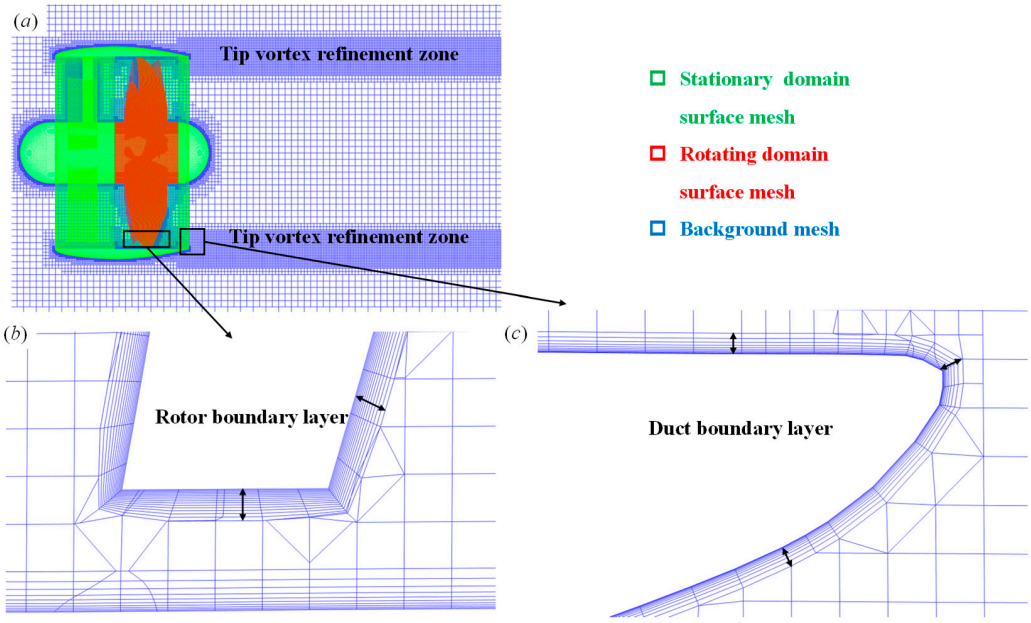


Figure 4. Mesh generation (**a**) and boundary layer details (**b**,**c**).

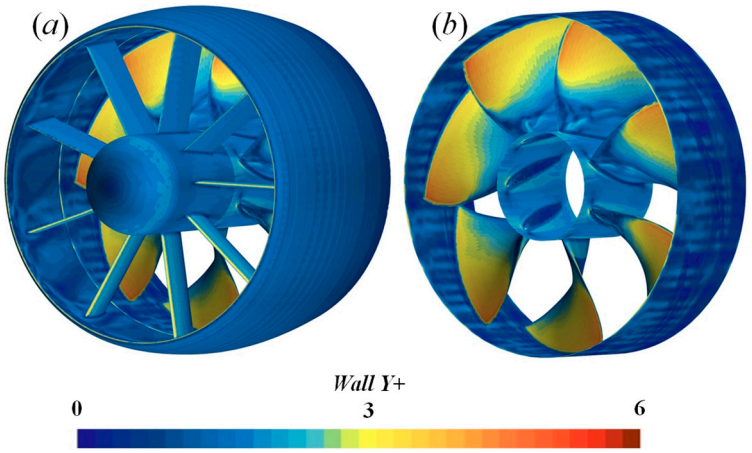


Figure 5. Wall Y+: (**a**) PJP, and (**b**) rotor.

3. Mesh Verification and Open-Water Validation

3.1. Mesh Convergence Verification

Prior to formal computations, the established numerical strategy needed to be validated. Three sets of grids—coarse, medium, and fine—were generated by systematically refining the base size with a refinement ratio of $\sqrt{2}$. The calculations were performed under the operating condition of n = 16 rps and V = 3.8 m/s (J = 1). The results obtained from the three grid sets are presented in Table 3. The thrust coefficient K_T is the total thrust coefficient, which comprises the rotor thrust coefficient K_{TR} and the combined thrust coefficient of the duct and stator K_{TD}. The torque coefficient is denoted by K_Q. These coefficients are presented as functions of the advance coefficient J. The corresponding expressions are given in Equations (8)–(11). By evaluating the simulation results across the different grids, no significant discrepancies were observed, indicating that all three mesh schemes lie within the asymptotic range of convergence.

$$J = \frac{V_a}{nD_R} \tag{8}$$

$$K_{TR} = \frac{T_R}{\rho n^2 {D_R}^4}, K_{TD} = \frac{T_D}{\rho n^2 {D_R}^4}, K_T = K_{TR} + K_{TD} \tag{9}$$

$$K_Q = K_{QR} = \frac{Q_R}{\rho n^2 {D_R}^5} \tag{10}$$

$$\eta = \frac{J}{2\pi}\frac{K_T}{K_Q}, \eta_R = \frac{J}{2\pi}\frac{K_{TR}}{K_{QR}} \tag{11}$$

Table 3. Computational mesh settings for different refinement levels.

	Base Size	Stationary Domain Mesh	Rotating Domain Mesh	K_{TR}	K_T	$10K_Q$	η
Coarse Mesh	0.07 m	4.04 M	3.71 M	0.4169	0.3420	1.0901	0.4993
Medium Mesh	0.05 m	7.82 M	6.46 M	0.4174	0.3424	1.0866	0.5015
Fine Mesh	0.035 m	13.23 M	17.49 M	0.4175	0.3425	1.0843	0.5027

To further validate the correctness of the numerical strategy, open-water tests of the pump-jet propulsor were conducted at the Shanghai Ship and Shipping Research Institute (SSSRI). The tests were performed in a ship model towing tank with the main dimensions of 192 m in length, 10 m in width, and 4.2 m in water depth. The towing carriage, driven by

a servo-controlled motor, achieves a speed range of 0.2~9 m/s. The towing tank is shown in Figure 6.

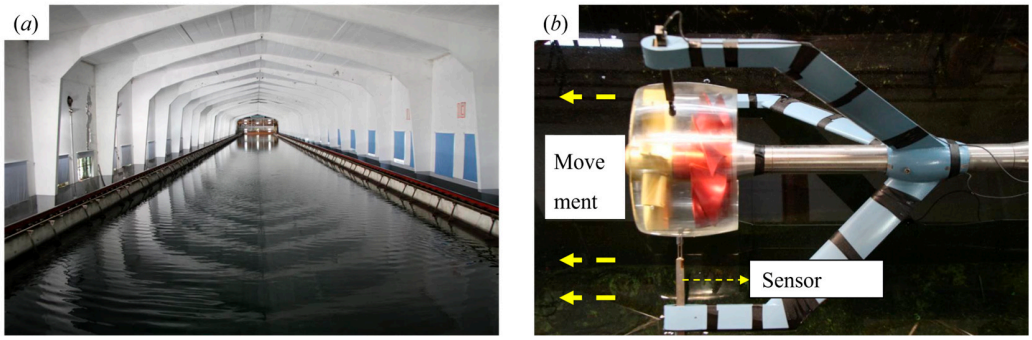


Figure 6. Schematic of the test facility: (**a**) towing tank, and (**b**) test model of the pump-jet propulsor.

The pump-jet model was mounted on an open-water dynamometer manufactured by the Maritime Research Institute Netherlands (MARIN), as shown in Figure 7. The MARIN dynamometer is capable of measuring a maximum thrust of 700 N and a maximum torque of 50 N·m. In addition, three single-component balances were employed to measure the combined thrust of the duct and stator. Each balance has a full-scale range of 20 kg and is oriented along the carriage travel direction, with the positive direction defined as the thrust direction. The rotor thrust was obtained by subtracting the duct-and-stator thrust from the total thrust measured by the MARIN dynamometer, thereby enabling the decomposition of the total thrust into the rotor thrust coefficient K_{TR} and the combined duct-and-stator thrust coefficient K_{TD}.



Figure 7. Open-water dynamometer.

The open-water tests adopted a constant-RPM method, in which the rotor rotational speed was maintained at a fixed value of n = 16 rps while the carriage speed was systematically varied to cover a range of advance coefficients J. At each carriage speed, the data acquisition system recorded the thrust, torque, and rotational speed signals over a steady-state duration to ensure statistical convergence. The measured raw signals were averaged over the steady-state interval to obtain the mean thrust and torque values at each operating point. The thrust coefficient K_T (including K_{TR} and K_{TD}) and the torque coefficient K_Q were then calculated from the net thrust and torque values at each advance coefficient J.

Throughout the entire advance coefficient range, the Reynolds number exceeded 4.5×10^5, which is above the critical value recommended by the ITTC for open-water tests, ensuring that the boundary layer flow over the blade sections was fully turbulent and that the test results were Reynolds-number independent.

3.2. Open-Water Validation

Figure 8 presents a comparison between the CFD-calculated results and the experimental data. The trends and magnitudes of the calculated curves show good agreement with the experimental values. The maximum error occurs in the torque coefficient at $J = 0.4$, while the errors for all coefficients remain below 4.5%. This calculation accuracy meets engineering requirements, further validating that the adopted numerical strategy is suitable for the pump-jet propulsor studied in this paper. Consequently, the predicted hydrodynamic performance results can serve as a reliable basis for the subsequent analysis and design optimization.

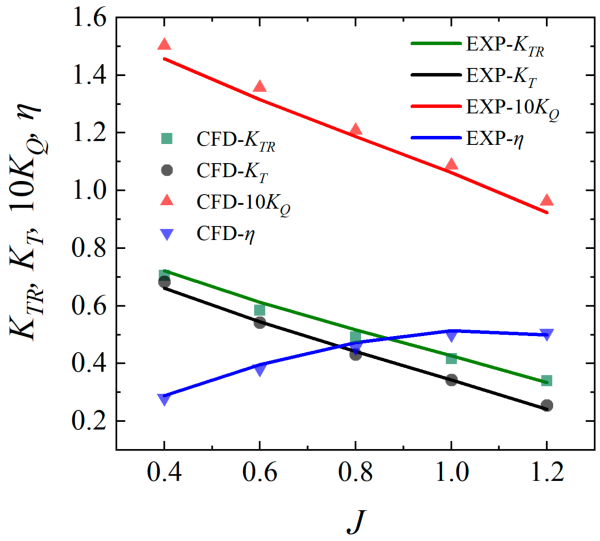


Figure 8. Comparison between computational and experimental results of pump-jet hydrodynamic performance.

4. Results and Discussion

4.1. Effect of the CLT Structure on the Hydrodynamic Performance of a Pump-Jet Propulsor

Figure 9 presents a comparison of the hydrodynamic performance between the various CLT pump-jet propulsors and the baseline prototype. An analysis of Figure 9a–c reveals significant differences at low advance coefficients. Compared to the prototype, the torque coefficient of the CW1 model shows a slight reduction at both low and high advance coefficients. The maximum percentage decrease (reduction ratio) of approximately 5% occurs at $J = 0.4$, while, at other higher advance coefficients, the reduction ratio is around 1%. However, this is accompanied by a loss in both the rotor thrust and overall thrust. At $J = 0.4$, both the rotor thrust coefficient and the overall thrust coefficient decrease by about 6%. At other higher advance coefficients, the reduction ratios range between 1% and 2%. Since the rotor thrust constitutes a major portion of the overall thrust, the fluctuation amplitudes of these two thrust coefficients are similar. Therefore, for subsequent discussions of other configurations, only the rotor thrust coefficient will be addressed. The maximum efficiency loss for the CW1 model within the range of $J = 0.4$–1.2 is 2%.

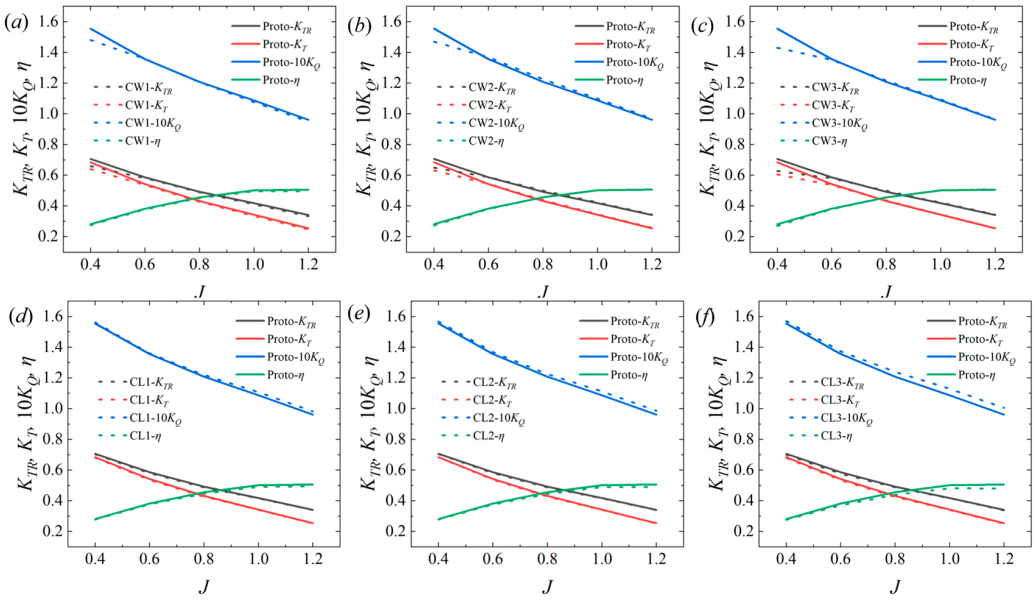


Figure 9. Comparison of hydrodynamic performance for (**a**–**c**) variable width (CW) series and (**d**–**f**) variable length (CL) series.

Compared to the prototype, the torque coefficient of the CW2 model decreases by about 5% only at J = 0.4. At other higher advance coefficients, it shows an increase with a percentage growth (increase ratio) of around 1%. The rotor thrust also incurs a loss only at J = 0.4, approximately 8%, while it shows a slight increase at other higher advance coefficients, with a maximum increase ratio of 1.6%. The efficiency of the CW2 model shows a marginal improvement at the maximum discussed advance coefficient of J = 1.2, while the average efficiency loss at other advance coefficients is less than 1%.

Compared to the prototype, the torque coefficient of the CW3 model decreases by about 8% only at J = 0.4. At other higher advance coefficients, the increase ratio is around 1%. The rotor thrust also shows a loss only at J = 0.4, approximately 11%, while it increases slightly at other higher advance coefficients, with a maximum increase ratio of 1.2%. The efficiency of the CW3 model shows an increasing trend within J = 0.8–1.2, with an average increase of about 1%, whereas it shows a decreasing trend within J = 0.4~0.8, with an average reduction of about 2%.

The installation of CW-type endplates has the most significant impact on the propulsor performance at J = 0.4. A smaller endplate width corresponds to a greater reduction ratio in the torque coefficient relative to the prototype, along with larger reduction ratios in thrust coefficient and efficiency. Therefore, when selecting a CW-series CLT pump-jet, a comprehensive consideration of the advance coefficient ranges where advantages in torque, thrust, and efficiency are manifested is necessary.

Regarding the endplate length, compared to the prototype, the torque coefficient of the CL1 model shows a slight increase across the entire range of advance coefficients discussed, with a maximum increase ratio of 2%. Both the rotor thrust coefficient and the overall thrust coefficient are also lower than those of the prototype, but the reduction ratio at each advance coefficient does not exceed 1%. The reduction ratio first increases and then decreases, peaking at J = 0.8. The efficiency reduction ratio becomes larger with an increasing advance coefficient, reaching a maximum of 2.5%.

The trends of the various propulsion coefficients for the CL2 and CL3 models are consistent with those of the CL1 model. The CL2 model shows a maximum torque coefficient increase ratio of 2.6% and a maximum efficiency reduction ratio of 3%. The CL3 model shows a maximum torque coefficient increase ratio of 4.5% and a maximum efficiency

reduction ratio of 5%. For the CL-series CLT pump-jet propulsors, the efficiency reduction ratio increases with higher advance coefficients. At the same advance coefficient, a larger endplate length leads to a greater efficiency reduction ratio.

4.2. Effect of the CLT Structure on the Vortical Flow Field of a Pump-Jet Propulsor (J = 1)

The flow within the internal and wake fields of a pump-jet propulsor is complex. The flow in the gap between the rotor tip and the inner wall of the duct directly affects both the propulsive and acoustic performance of the propulsor. This section will analyze the characteristics of the gap flow in detail and summarize the influence of the endplate. During high-speed rotation, a relative motion is formed between the rotor and the duct inner wall, causing part of the fluid to flow back from the pressure side to the suction side and resulting in complex tip gap flow [25,26]. Figure 10 presents the vorticity contours of the gap flow field for the baseline rotor and the CLT-type rotor at J = 1.0. The figure shows the rear part of the tip section of the leading blade (Rotor1) and the entire tip section of the following blade (Rotor2). Observing Figure 10a, the tip leakage vortex (TLV) is shed from the mid-to-aft section of the chord and develops downstream into the rotor passage. It interacts and merges with the main flow within the passage, leading to a gradual decrease in the TLV core strength. During its downstream development, the TLV interacts with the pressure surface of the following blade, influencing the rotor performance. On the same cross-section, the vortex core strength of the tip separation vortex (TSV) is significantly lower than that of the TLV. The development path (trajectory) of the TSV largely aligns with the skew angle of the rotor blade.

Observing Figure 10b–d for the variable endplate width series, the angle between the TLV development path and the rotor blade chordwise direction decreases. As the endplate width narrows, the vortex core strength of the TLV shed at each cross-section increases overall, while the vortex core strength of the TLV developing downstream into the rotor passage decreases overall. The variation in endplate width shows no observable effect on the shedding location of the TLV or on the angle between the TSV development path and the blade.

Observing Figure 10e–g for the variable endplate length series, the tip of the baseline rotor itself is flat-ended. Since the endplates in this series are bent 90° relative to the main blade tip, modifying only the endplate length essentially extends the rotor tip surface towards the pressure side. The overall development paths of the TLV for the three CL rotor models are similar to that of the baseline rotor. The vortex core strength of the TLV at each cross-section increases overall. With the increasing endplate length, the axial extension distance of the vortex structure shortens. The TLV of the CL3 model shows almost no axial extension, shedding directly downstream in the rotational direction, resulting in relatively less loss of vortex core strength. In summary, longer endplates lead to a weakened axial extension of the TLV, increased TLV vortex core strength, and diminished TSV vortex intensity.

To further compare the tip vortex characteristics of the various pump-jet propulsors, the vorticity contour plots of the overall flow field at J = 1.0 are extracted, with the results shown in Figure 11. Observing the vorticity distribution of the baseline pump-jet propulsor, the duct trailing vortex and the rotor-shed vortex can be clearly identified in the near-wake region. The interaction between these two vortices generates secondary vortical structures. As they develop downstream, they gradually enter an unstable stage, beginning to destabilize, break down, and fragment [27,28].

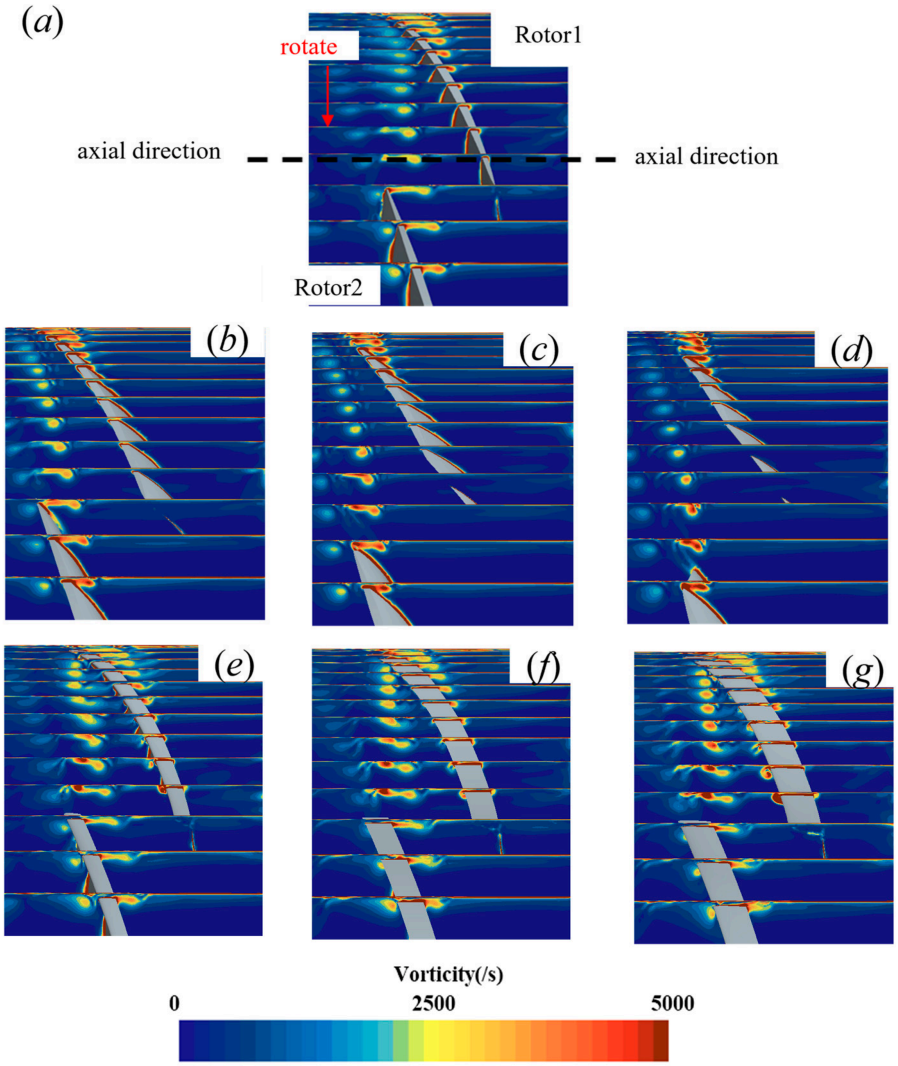


Figure 10. Vorticity distribution in the gap region for all pump-jet models (J = 1): (**a**) baseline, (**b**–**d**) variable width (CW) series, and (**e**–**g**) variable length (CL) series.

Observing Figure 11b–d for the variable width series, the onset of the vortex system's unstable stage is delayed. A smaller endplate width corresponds to a longer persistence of the spiral-shaped tip vortices shed from the rotor, with the breakdown and fragmentation phenomena occurring later. The vortex intensity of the CW1 model dissipates most rapidly. Due to the installation of the CW-type endplate, the radial disturbance to the downstream vortices is weakened, and its influence on the duct trailing vortex is also reduced. This allows the duct trailing vortex to develop over a longer distance, slowing its energy dissipation. Observing Figure 11e–g for the variable length series, longer endplates lead to a weakened radial dissipation of the secondary vortices, resulting in a more stable vortex development and a more gradual dissipation of the vortex core intensity. Compared to the baseline, the CL1 model shows little change in the vortex core intensity and its dissipation during development. The CL3 model exhibits a more continuous and stable vortex system development, with minimal interaction between the duct trailing vortex and the rotor-shed vortex, leading to a slower dissipation of the vortex intensity.

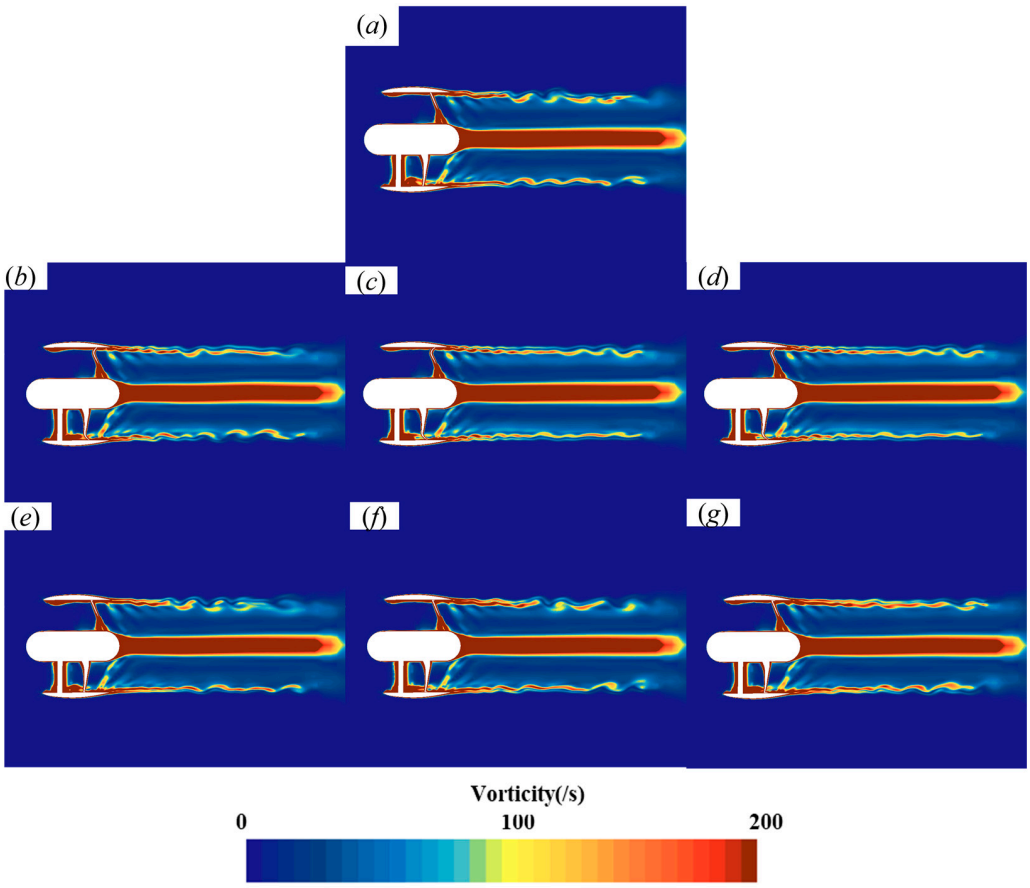


Figure 11. Vorticity distribution for all pump-jet models (J = 1): (**a**) baseline, (**b**–**d**) variable width (CW) series, and (**e**–**g**) variable length (CL) series.

4.3. Analysis of the Influence of the CTL Structure on Pulsating Pressure in a Pump-Jet Propulsor (J = 1)

To investigate the influence of the endplate structure on the overall flow field and the gap flow field, fluctuating pressure monitoring points were arranged within the internal and external flow fields of the pump-jet propulsor. The specific locations are shown in Figure 12. After the preliminary screening of the monitored data, the analysis presented in the following sections focuses on the pressure coefficient monitoring results from four rotational periods in the steady-state phase at the stator inlet section, the mid-section between the stator and rotor, the radial profile at the rotor tip, and the rotor outlet section.

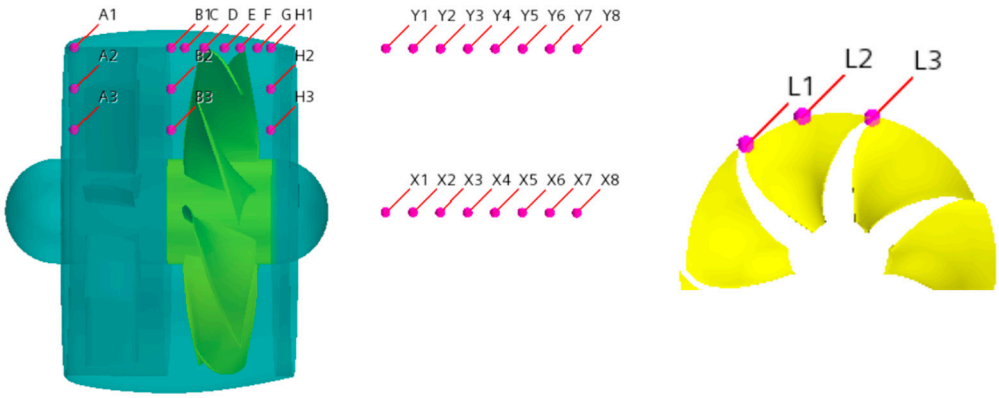


Figure 12. Schematic diagram of the acoustic monitoring points arrangement for the pump-jet propulsor.

Figure 13 shows the time-domain pressure fluctuations at each monitoring point for the baseline pump-jet propulsor. At the stator inlet section, point A1, located near the inner wall of the duct, exhibits the largest fluctuation amplitude. The amplitudes at points A2 and A3, situated at the mid-radius and near the hub respectively, are smaller. On this section, the pressure fluctuations at the monitoring points do not show a clear periodic nature.

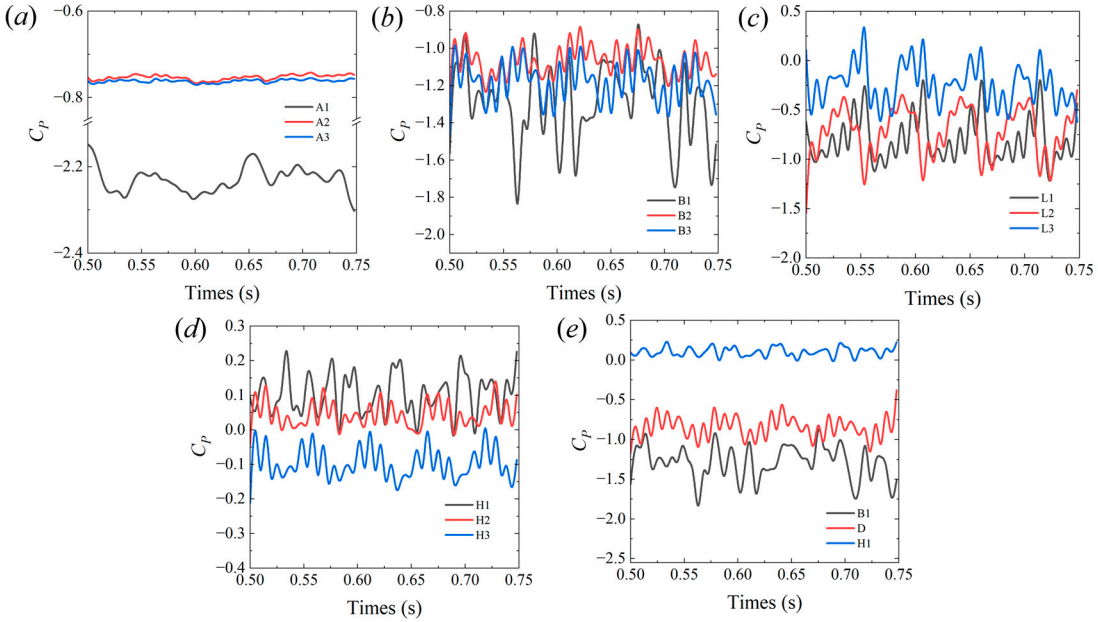


Figure 13. Comparison of time-domain pressure fluctuations at monitoring points for the baseline pump-jet propulsor (**a**) Front cross-section of the stator (**b**) Intermediate cross-section between the stator and rotor (**c**) Radial profile at the rotor tip (**d**) Rear cross-section of the rotor (**e**) Uniform monitoring points arranged in the gap between rotor and duct.

At the mid-section between the stator and rotor, point B1, near the duct inner wall, shows the largest pressure fluctuation amplitude, while point B2 at the mid-radius shows the smallest. On this section, the pressure fluctuations near the duct inner wall still lack obvious periodicity. At the radial profile of the rotor tip, point L1 at the leading edge exhibits the largest pressure fluctuation amplitude, and point L3 at the trailing edge shows the smallest. Due to the disturbance caused by rotor rotation, all three monitoring points here display distinct periodicity. At the rotor outlet section, point H1 near the duct inner wall has the largest pressure fluctuation amplitude, and point H2 at the mid-radius has the smallest. Comparing the monitoring points on the sections upstream and downstream of the rotor, it is evident that all points on the downstream section exhibit periodicity. The rotor has a significant influence on the pressure fluctuations near the duct inner wall. An analysis of the monitoring points at uniform intervals within the gap between the duct and rotor shows that point B1, located upstream of the rotor, has the largest amplitude, while point H1, downstream of the rotor, has the smallest. Point D, located at the axial position of the rotor, exhibits the most pronounced periodicity.

Figure 14 presents the frequency-domain pressure fluctuations at the monitoring points for both the baseline pump-jet propulsor and the CLT-type propulsors. In this section, the Abs amplitude function of the Fast Fourier Transform (FFT) was employed to convert the time-domain fluctuating pressure into frequency-domain data for analysis. Observing the frequency-domain distribution of the baseline pump-jet propulsor in Figure 14a, rich spectral features are evident at the blade frequency (112 Hz) and its harmonics within the analyzed frequency range. The peaks at the blade frequency for monitoring points located both upstream and downstream of the rotor are relatively small, and the spectral

characteristics diminish at higher frequencies. At the rotor tip profile section, the spectral characteristics within the analyzed frequency range are more pronounced. The spectrum at the leading edge point L1 is the most feature-rich, while the characteristic peak at the trailing edge point L3 is the largest in magnitude. However, the peak amplitudes in higher frequency bands are relatively small. Corresponding to its time-domain distribution, point L1 consequently exhibits a larger amplitude of time-domain pressure fluctuation.

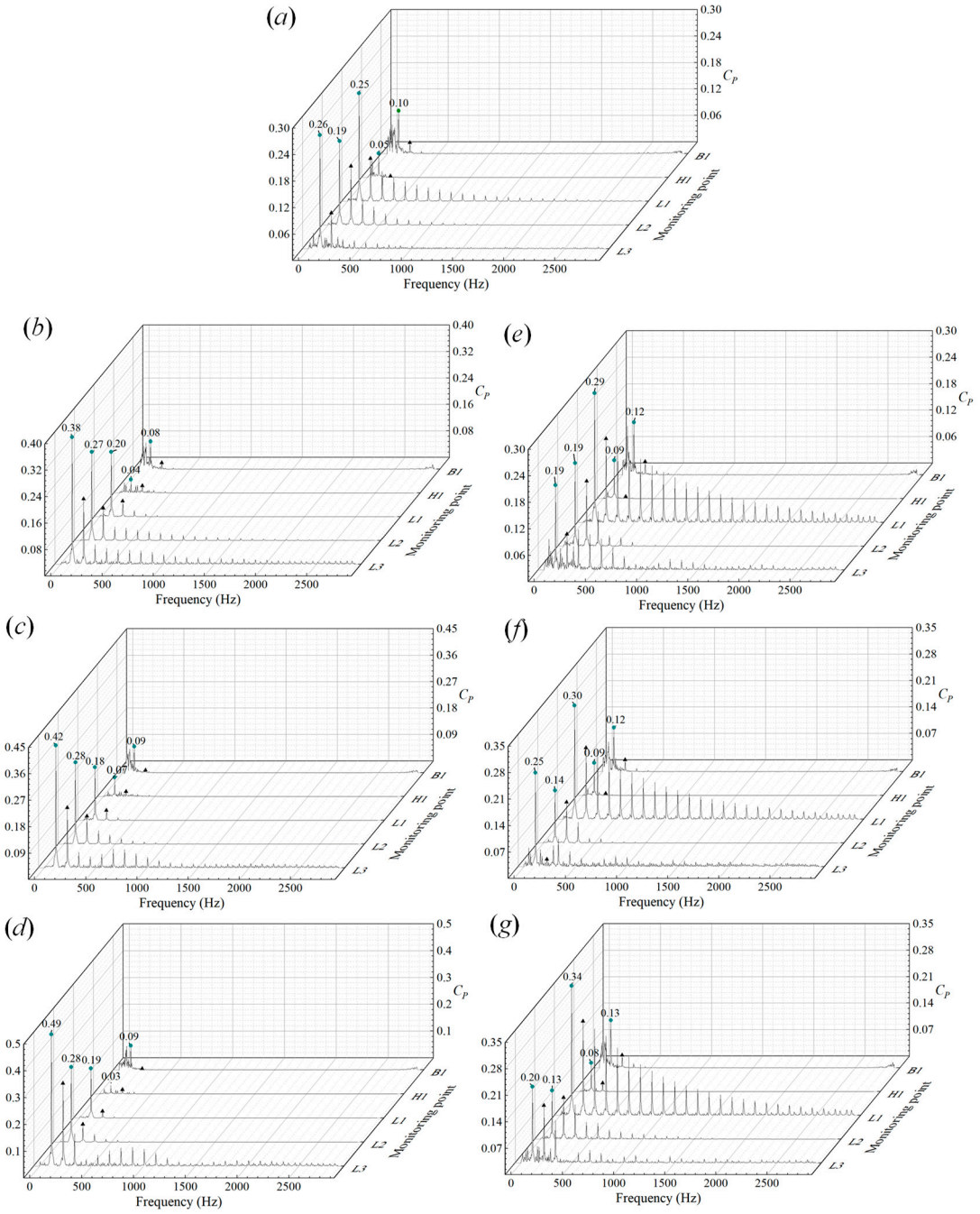


Figure 14. Comparison of frequency-domain pressure fluctuations at monitoring points for various pump-jet models: (**a**) baseline, (**b**–**d**) variable width (CW) series, and (**e**–**g**) variable length (CL) series.

Figure 14b–d present the frequency-domain pressure fluctuations at the monitoring points for the variable endplate width series. Compared to the baseline pump-jet, the characteristic peak at point L3 becomes the largest and exhibits the richest spectral features. Considering the geometric changes in the rotor, the monitoring points are fixed three-

dimensional coordinates within the flow field set based on the tip profile of the baseline rotor blade. Consequently, the monitored profile positions for these three points have shifted, leading to significant changes in their characteristic distributions. As the endplate width decreases, the characteristic peak at the blade frequency and the overall spectral characteristics at point B1 (upstream of the rotor) show little change. The characteristic peak at the blade frequency at point H1 (downstream of the rotor) first increases and then decreases. The overall spectral characteristics at point L2 on the rotor tip profile continuously weaken, while the characteristic peak at the blade frequency at point L3 consistently increases, with a maximum difference of 0.23 compared to the baseline pump-jet peak value. Although the CW-type designs show limited suppression effectiveness at the blade frequency itself, their inhibitory effect becomes more pronounced at the other blade-passing harmonics as the endplate width decreases. This is particularly evident for the CW3 model, where points L1 and L2 exhibit distinct peaks only at the first and second blade-passing frequencies, with a decrease in average amplitude. This indicates that, for CW-type rotors, adjusting the endplate width can effectively mitigate tip vortex-induced vibration.

Figure 14e,f present the frequency-domain pressure fluctuations at the monitoring points for the variable endplate length series. Compared to the baseline pump-jet, the overall spectral characteristics at each monitoring point are relatively similar. Due to the installation of the CL-series endplates, the characteristic peak at the blade frequency at point B1 (upstream of the rotor) is larger than that of the baseline pump-jet. Variations in endplate length have little effect on the characteristic peak or the overall spectral characteristics at point B1. At point H1 (downstream of the rotor), the characteristic peak at the blade frequency increases, with minimal influence from changes in endplate length. At point L1 (the leading edge on the rotor tip profile), compared to the baseline pump-jet, the characteristic peaks at the blade-passing harmonics are significantly larger. Furthermore, longer endplates correspond to greater peak amplitudes at these harmonics. When longer endplates are installed, the characteristic peak at the blade frequency at point L2 on the rotor tip profile decreases. The spectral characteristics of the CL2 model are notably weakened. At point L3 (the trailing edge), the characteristic peaks at the blade-passing harmonics are significantly reduced. The CL1 model exhibits the smallest characteristic peak at the blade frequency.

4.4. Analysis of the Influence of the CTL Structure on Noise in a Pump-Jet Propulsor (J = 1)

The operating condition of $J = 1.0$ was selected for computational analysis. The Ffowcs Williams–Hawkings (FW-H) acoustic analogy was employed to solve the acoustic field of the pump-jet propulsor [29]. The time step was set to 0.00025 s, enabling analysis up to a frequency of 2000 Hz. The surface of the pump-jet propulsor was defined as the noise source location. Based on underwater acoustic field characteristics, the far-field density was set to 997.561 kg/m^3 and the far-field sound speed to 1500 m/s. After the flow calculation converged, the time-domain data of the overall sound pressure at the monitoring points were extracted. These data were converted to the frequency domain via FFT, with a reference sound pressure of $p_0 = 1 \times 10^{-6}$ Pa. This reference value is the standard reference sound pressure for underwater acoustics [30], which is conventionally adopted for underwater noise evaluation.

For calculating the noise of a single pump-jet propulsor, acoustic monitoring points were placed at distances of 1 m and 20 m from the geometric center of the rotor. The circumference of both the radial and axial planes was divided into 12 equal segments. The radial plane was located at the propeller disk plane. Among these, the A1 point direction corresponds to the axial monitoring point toward the stern, and the A4 point direction corresponds to the radial monitoring point in the rotor disk plane. The acoustic

monitoring points are shown in Figure 15. It should be noted that Figure 15 only illustrates the monitoring point arrangement at the near-field distance of 1 m. The same naming convention and relative spatial positions are adopted for the far-field monitoring points at 20 m, with only the distance from the pump-jet propulsor increased.

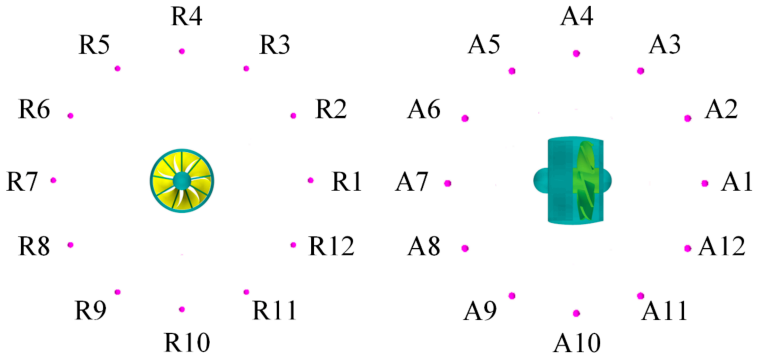


Figure 15. Acoustic monitoring points under uniform inflow (**left**: radial plane; **right**: axial plane).

Figures 16 and 17 present comparative spectrograms of the sound source levels between the CLT pump-jet propulsors with different parameters and the baseline pump-jet propulsor. Theoretically, with a shaft frequency of 16 Hz and a 7-bladed rotor, the blade-passing frequency is 112 Hz, which is marked by the red vertical lines in the spectrograms. The numerical results are observed to agree well with these theoretical characteristics. Comparing the spectral characteristics at the same axial position but different distances, at position A1, tonal noise dominates and contributes significantly to the sound source level in the low-frequency range below 0.5 kHz. The broadband noise in the higher frequency range gradually decays with increasing frequency and contributes little to the overall sound pressure. At position A4, broadband noise dominates, and the sound source levels in the higher frequency range are notably and generally higher. Comparing the spectral characteristics at different circumferential positions but the same distance, at both 1 m and 20 m distances, the peak sound source level value at point A1 is higher than that at point A4. At the 1 m distance, the peak sound source level occurs at the fundamental blade-passing frequency (112 Hz). At the 20 m distance, the peak sound source level shifts to a higher harmonic frequency. As the monitoring distance increases, the spectral features weaken slightly, particularly with minor differences observed in the discrete tonal lines within the low-frequency range.

Figure 16 presents a comparison of the sound source level spectra on the axial plane between the baseline propulsor and the variable endplate width series. At the same distance and circumferential position, the four propulsor types share identical characteristic frequencies. Their spectra all consist of discrete tonal noise, represented by the shaft frequency, blade-passing frequency, and their harmonics, as well as broadband noise, although differences exist in the peak frequencies. In subfigures (a) and (c), at circumferential position A1, the sound source level peaks for the variable width series within the frequency range of $2f_n$~1 kHz are generally lower than those of the baseline. This trend persists with increasing distance. In subfigures (b) and (d), at circumferential position A4, the sound source level peaks for the variable width series do not show a significant reduction, and their spectral shapes and amplitudes are similar to those of the baseline.

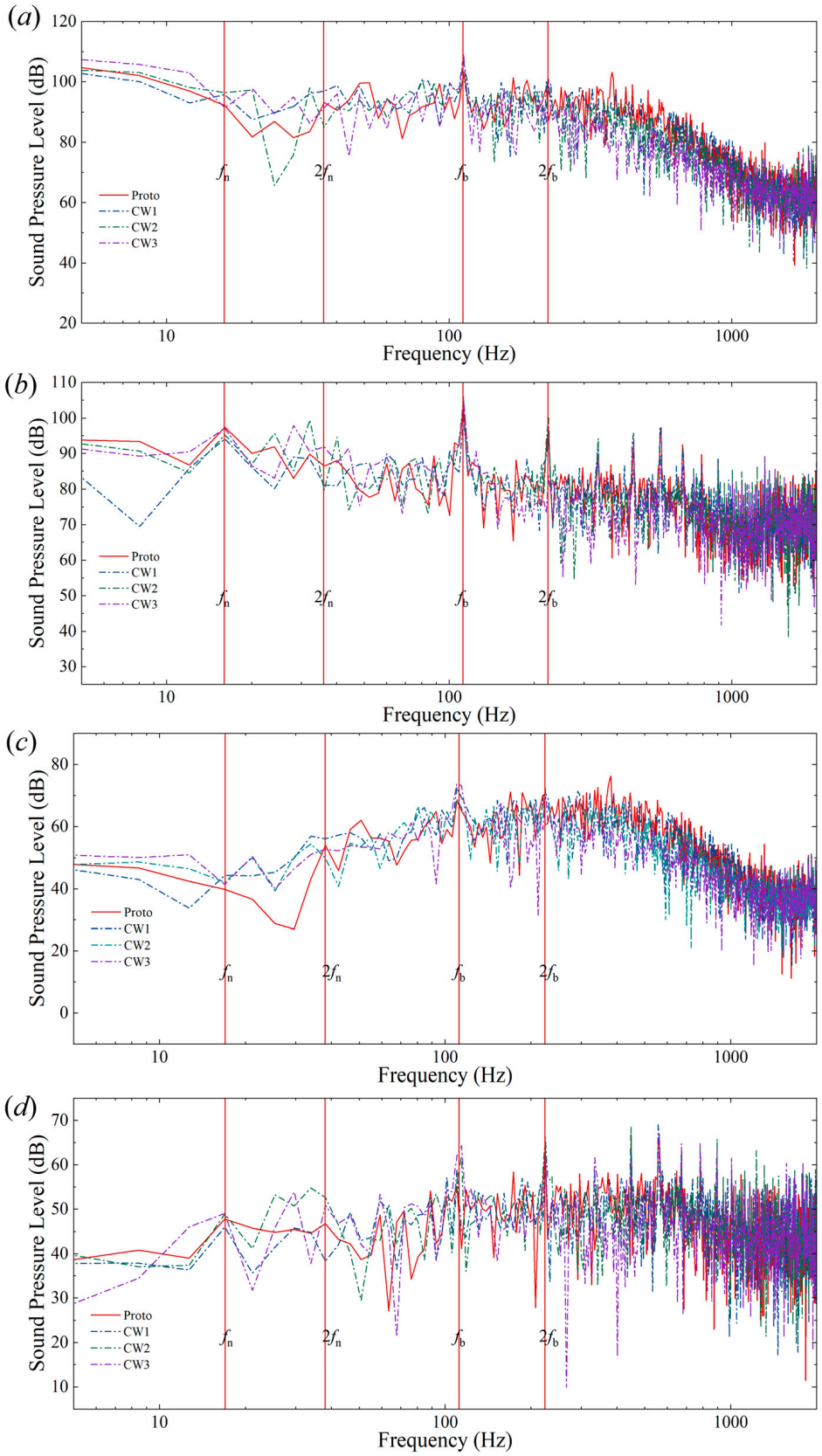


Figure 16. Comparison of the sound source level spectra on the axial plane between the baseline and variable width (CW) series: (**a**,**b**) results at near-field positions 1 m-A1 and 1 m-A4; and (**c**,**d**) results at far-field positions 20 m-A1 and 20 m-A4 (f_n = 16 Hz, f_b = 112 Hz).

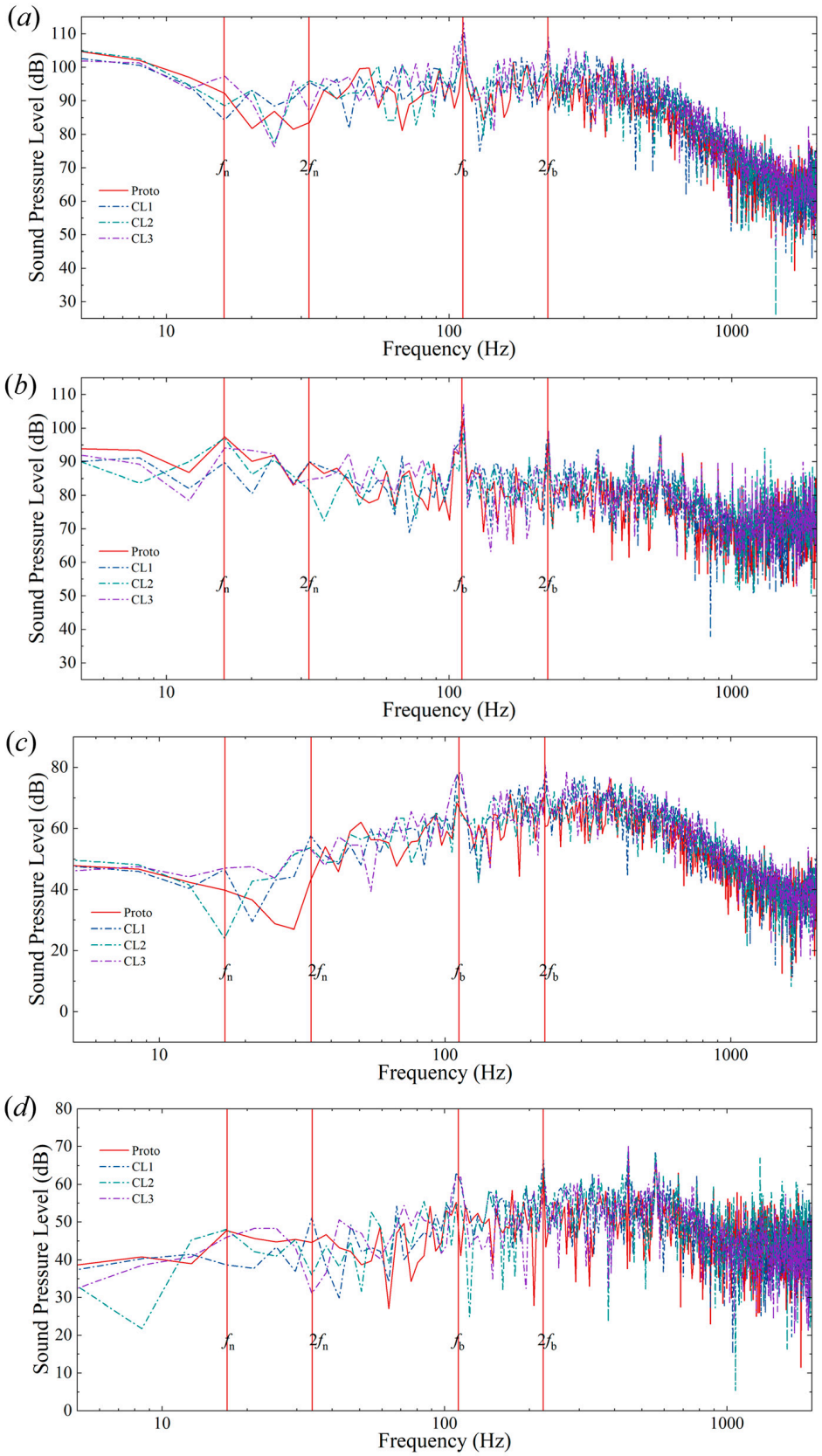


Figure 17. Comparison of the sound source level spectra on the axial plane between the baseline and variable length (CL) series: (**a**,**b**) results at near-field positions 1 m-A1 and 1 m-A4; and (**c**,**d**) results at far-field positions 20 m-A1 and 20 m-A4 (f_n = 16 Hz, f_b = 112 Hz).

Figure 17 presents a comparison of the sound source level spectra on the axial plane between the baseline propulsor and the variable endplate length series. The overall spectral characteristics of the three CLT-type pump-jet propulsors remain consistent with those of the baseline model, comprising discrete tonal noise, represented by the shaft frequency, blade-passing frequency, and their harmonics, as well as broadband noise. However, minor differences are observed in the discrete tonal components at each monitoring point. At the 1 m-A1 position and at the fundamental blade-passing frequency f_b, the sound source levels of the CL1 and CL3 models are higher than that of the baseline, while the CL2 model is slightly lower. The maximum difference Δf is approximately +10 dB (for the CL3 model). As the monitoring distance increases to the 20 m-A1 position, the peak sound source level of the baseline and the CL2 model shifts to a higher harmonic frequency, whereas the peak levels of the CL1 and CL3 models remain at the fundamental blade-passing frequency f_b. At the 1 m-A4 position, the spectral characteristics of the sound source level for the baseline and the CLT models are similar. At the fundamental blade-passing frequency f_b, where the peak sound source level occurs, the CL3 model is about 4 dB higher than the baseline, and the CL2 model is about 4 dB lower. At the 20 m-A4 position, within the frequency range from f_n~$2f_b$, the discrete tonal noise characteristics of the baseline and the CL2 model are quite similar, as are those of the CL1 and CL3 models. For all four models, the peak sound source level shifts to a higher harmonic frequency.

Figure 18 illustrates the directivity of the overall sound source level for the baseline pump-jet propulsor on both the axial and radial planes. On the axial plane, the overall sound source level contours at distances of 1 m and 20 m approximate an ellipse, with the axial sound source level being greater than the radial level. Pronounced variations in values are observed in the forward/aft (A7, A1) and above/below (A4, A10) directions of the propulsor. At the 1 m distance, the two extreme values are located at A4 and A2, with a difference of 4.9 dB. At the 20 m distance, the locations of the extreme values remain the same as at 1 m, but the difference increases to 21 dB. As the monitoring distance increases, the difference between the extreme values grows significantly. The minimum value points are located above and below the propulsor, which is considered an advantageous effect attributable to the pump-jet duct. On the radial plane, the overall sound source level contours at both 1 m and 20 m distances are nearly circular. The overall sound source level at each point approximates the values measured above and below on the axial plane, exhibiting only slight or almost no directivity. At the 1 m distance, the two extreme values are located at R9 and R3, with a difference of 1.4 dB. At the 20 m distance, the two extreme values are located at R1 and R7, with a difference of 1 dB.

Since the directivity of the overall sound source level on the radial plane is not pronounced, and the values at all points differ from those at the above/below monitoring points (A4 and A10) on the axial plane by approximately 1 dB, the subsequent analysis will primarily focus on the directivity of the overall sound source level on the axial plane. Figure 19 presents a comparison of the overall sound source level directivity on the axial plane between the baseline model and the variable endplate width series. The overall sound source level of the variable width series is lower than that of the baseline at most monitoring points, and this noise reduction effect becomes more pronounced with increasing distance. At the 1 m distance, at circumferential positions A3, A5, A9, and A11, the overall sound source level of the variable width series is higher than that of the baseline. The differences for the CW1 model range from +2.5 dB to +5.1 dB, for CW2 from +3 dB to +7.1 dB, and for CW3 from +2.3 dB to +6.4 dB. At all other axial positions, the overall sound source level of the variable width series is lower than the baseline. The maximum reduction for CW1 is −4.8 dB, for CW2 is −5.5 dB, and for CW3 is −5.7 dB, all occurring at point A2. At the 20 m distance, the noise optimization effect at the two points on the central axis (A1 and A7) is

more significant compared to the 1 m distance. Comparing the peak overall sound source level of each model, the CW3 model shows a reduction of approximately 4 dB relative to the baseline. In summary, the variable endplate width series exhibits a certain degree of optimization in noise performance. This effect is particularly evident at the longer distance of 20 m, which holds positive significance for practical engineering applications.

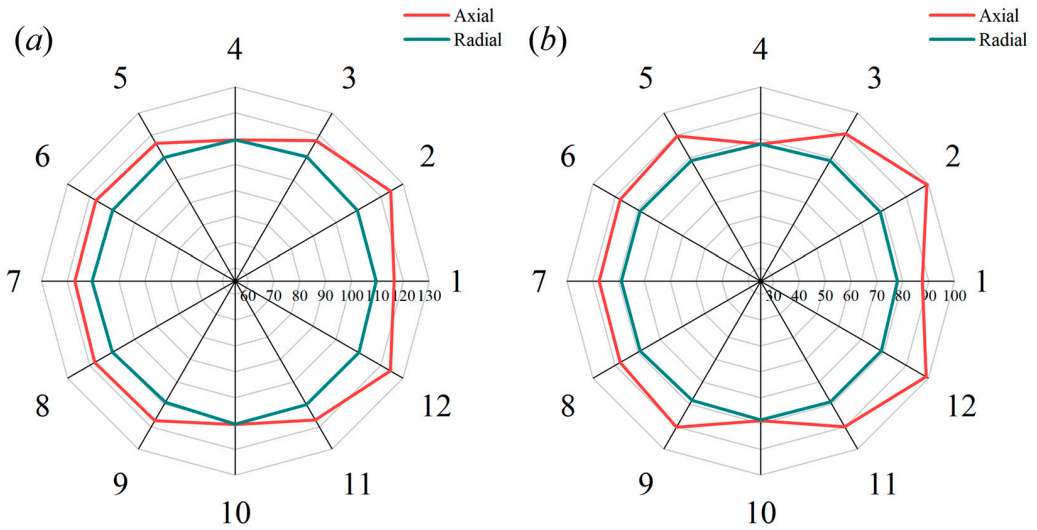


Figure 18. Overall sound source level directivity on the axial and radial planes for the baseline pump-jet propulsor (**a**) 1 m, (**b**) 20 m.

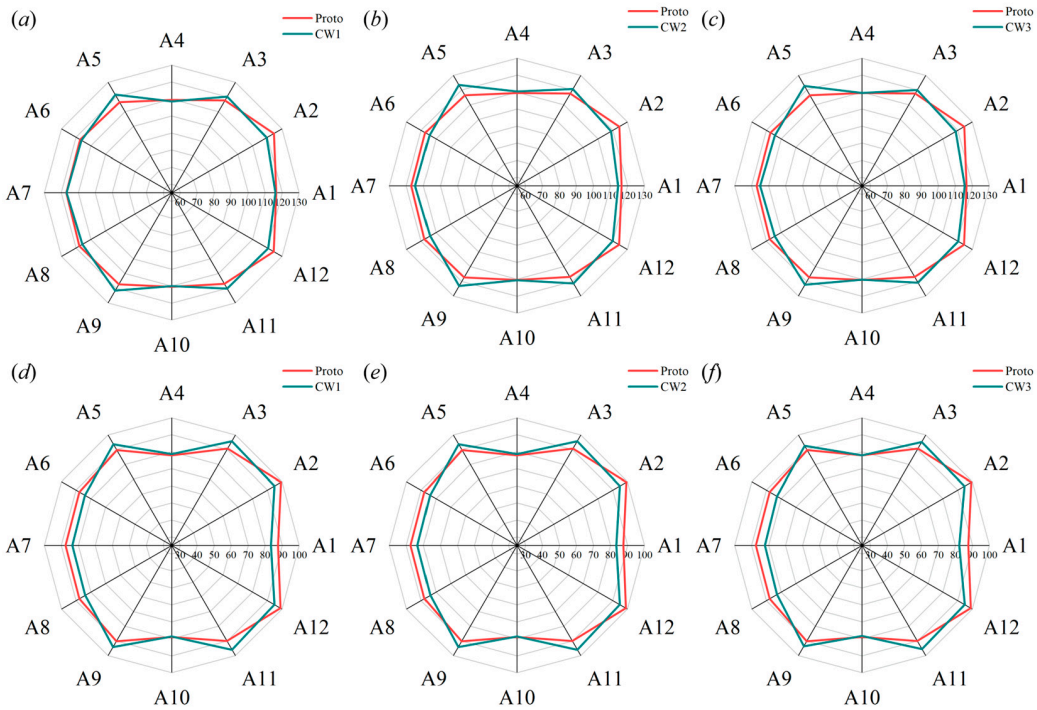


Figure 19. Comparison of overall sound source level directivity on the axial plane between the baseline and variable width (CW) series: (**a**–**c**) comparison results at near-field (1 m); and (**d**–**f**) comparison results at far-field (20 m).

Figure 20 presents a comparison of the overall sound source level directivity on the axial plane between the baseline model and the variable endplate length series. A comparison was made regarding the distribution pattern and magnitude of the overall sound source level. Compared to the baseline, the variable length series showed only a

marginal effect at the circumferential position A12. Overall, no significant noise reduction effect was observed for this series. Furthermore, with regard to the increase in monitoring distance, no optimization effect was identified either. A comparison of the overall sound source level among the three CLT-type pump-jet propulsors indicates that, at both the 1 m and 20 m distances, the CL2 model exhibits the lowest values across all monitoring points, making it the closest to the baseline model.

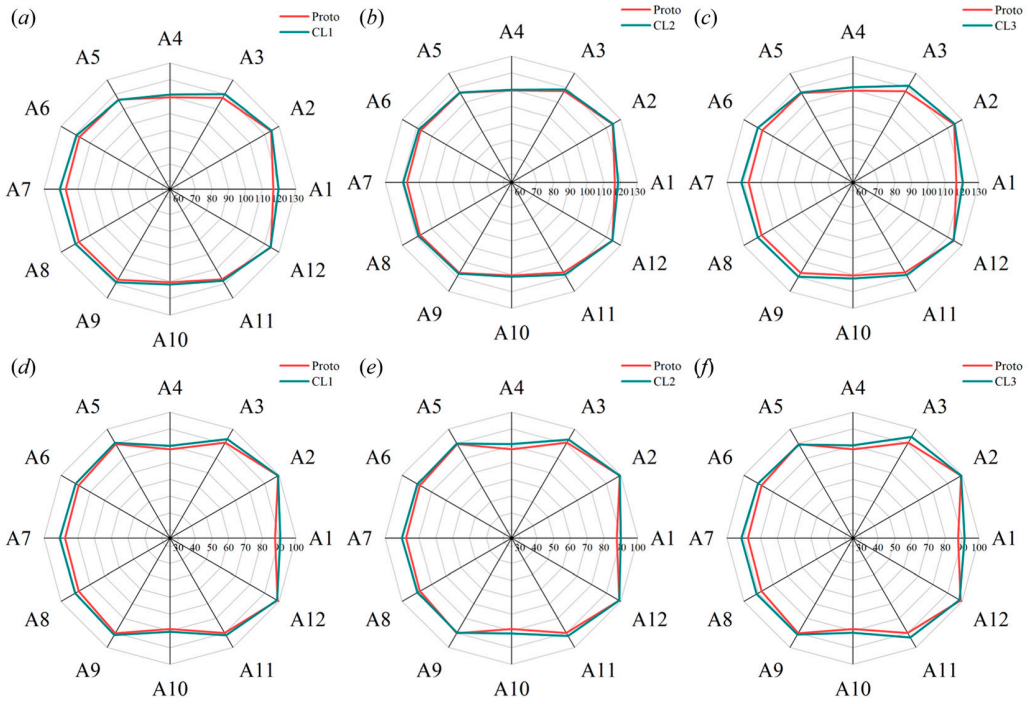


Figure 20. Comparison of overall sound source level directivity on the axial plane between the baseline and variable length (CL) series: (**a**–**c**) comparison results at near-field (1 m); and (**d**–**f**) comparison results at far-field (20 m).

For the CW-series CLT pump-jet propulsors, reducing the end-plate width decreases the intersection angle between the TLV development trajectory and rotor blades, which weakens the interference of TLV on the downstream rotor blades and suppresses flow-field pressure pulsations. Smaller end-plate width yields the stronger suppression of pressure pulsations at higher harmonic blade-passing frequencies. As the unsteady pressure pulsations on the rotor and duct surfaces serve as dominant dipole noise sources for non-cavitation noise, the alleviated pressure fluctuation leads to noise reduction. Nevertheless, this behavior is advance-ratio-dependent; CW configurations suffer thrust and torque degradation under low advance-speed conditions.

For the CL-series with an increased end-plate length, although the large-scale vortex structure becomes more stable and vortex fracture is delayed, the TLV vortex-core intensity is increased near the rotor tip. TLV tends to shed toward the rotational downstream instead of developing along the axial direction, which strengthens the interaction between TLV and subsequent rotor blades and elevates pressure-pulsation amplitudes on both the rotor blades and the inner duct wall. In addition, CL-series configurations generate higher torque coefficients, particularly at high advance coefficients, which further excites unsteady load fluctuations on blade surfaces. Since pump-jet non-cavitation noise is dominated by dipole sources induced by wall pressure pulsations, the aggravated pressure fluctuations counteract the benefit from macroscopic vortex stabilization. As a result, virtually no noise-reduction effect can be observed for CL-type pump-jet propulsors.

Taken together, the above parametric results reveal the competing trade-offs among the hydrodynamic performance, vortex evolution, and acoustic characteristics for CLT-type endplate configurations. Narrower endplates achieve a favorable noise-reduction performance at the cost of the deteriorated thrust-torque performance. By contrast, longer endplates stabilize vortex structures; yet, they mainly degrade the efficiency under high advance-coefficient conditions and intensify pressure fluctuations without producing noise-reduction benefits. From an engineering perspective, the variable-width CLT configuration shows greater potential for the low-noise pump-jet rotor design, whereas the accompanying efficiency penalty should be carefully balanced in practical applications. The present findings can offer preliminary guidance for the tip structural modification of pump-jet propulsors.

5. Conclusions

Based on the performance advantages of CLT propellers and the existing research on effective structural modifications for pump-jet rotors, a CLT-type pump-jet propulsor is proposed in this study. This design incorporates the CLT-type endplate structure onto the blade tips of the baseline pump-jet rotor. A parametric study is conducted, varying the inclination angle, width, and length of the endplate. Employing the DES method and the FW-H acoustic analogy equations, numerical simulations are performed for both the baseline and the CLT-type pump-jet propulsors. The study summarizes the hydrodynamic and acoustic performance characteristics of the baseline pump-jet propulsor and provides a comparative analysis of the performance optimization and characteristic trends observed in the CLT-type propulsors. The conclusions of this paper are as follows:

(1) The endplate width significantly affects the hydrodynamic performance of the pump-jet propulsor. Narrower endplates reduce the torque coefficient, thrust coefficient, and efficiency more substantially, thus requiring a trade-off between hydrodynamic efficiency and other benefits. The endplate length mainly influences the performance at higher advance coefficients, where increasing the length leads to more pronounced efficiency reduction.

(2) The TLV dominates over the TSV in the rotor–duct gap. The endplate geometry effectively modifies the evolution of these vortices: CW-type endplates increase the TLV core intensity near the blade tip but reduce it downstream, while CL-type endplates stabilize the axial development of the TLV and weaken the TSV. Narrower endplates prolong the stable development stage of wake vortices, and longer endplates delay vortex breakdown.

(3) Varying the endplate width suppresses pressure fluctuations and reduces noise, with a stronger effect for narrower widths. The best-performing model achieves maximum overall sound source level reductions of 5.7 dB at 1 m and 4.0 dB at 20 m. In contrast, varying the endplate length does not provide significant noise reduction. The acoustic directivity is elliptical on the axial plane and nearly circular on the radial plane.

The present work has several inherent limitations. The parametric test matrix adopts a one-factor-at-a-time strategy, and the variable-width and variable-length endplate series adopt non-overlapping tip rake values. Cross-combination geometric cases with mixed endplate width and rake parameters are absent, which prevents the complete decoupling of the respective quantitative contributions of the endplate width and rake inclination. Furthermore, the number of geometric variants is limited, making it difficult to generalize universal quantitative laws for the hydrodynamic and acoustic characteristics of CLT-type pump-jet propulsors. In addition, the numerical model involves certain simplifications: the flow is treated as incompressible and single-phase without cavitation, and the FW–H acoustic analogy with impermeable surfaces neglects flow–acoustic coupling. Another

important limitation originates from the scale effects. All simulations are performed under model-scale conditions consistent with laboratory tests. Complex scale-dependent physical phenomena, including Reynolds-number-dependent tip-gap flow evolution, boundary-layer development, and cavitation inception characteristics, will produce quantitative deviations when extrapolating model-scale results to full-scale propellers. Although the underlying vortex-modification physical mechanisms of CLT end-plates remain qualitatively valid at full scale, the magnitude of noise-reduction benefits and hydrodynamic performance penalties cannot be directly transferred. Hence, the optimal geometric parameters derived from model-scale computations cannot be directly adopted for full-scale engineering designs. Future work will supplement cross-combination parametric cases and expand the geometric sample space, so as to further clarify the coupling mechanism of endplate geometric parameters, identify possible critical values beyond which the CLT construction becomes unprofitable, and obtain more generalized performance variation rules.

Despite these limitations, the scientific novelty of this work lies in the first application of the CLT-type endplate structure to a pump-jet rotor and the systematic analysis of how endplate width and rake affect the hydrodynamic and acoustic performance of a ducted pump-jet propulsor.

The present DES–FW–H numerical strategy can be applied to propellers of different dimensions and purposes, provided that the flow remains incompressible and cavitation-free and the grid resolution is adjusted accordingly. However, the quantitative trends obtained here are geometry-specific; extrapolation to substantially different geometries should therefore be made with caution and supported by additional validation. The qualitative mechanisms identified in this study, particularly the effect of endplate width on tip vortex evolution and pressure fluctuations, are expected to provide useful guidance for other tip-loaded or ducted propulsors. Compared with RANS-based approaches and previously reported configurations, the present DES–FW–H strategy resolves the tip leakage vortex more directly, and the optimized CLT-type rotor achieves a maximum overall sound source level reduction of 5.7 dB at 1 m with limited efficiency loss.

Author Contributions: Methodology, Y.Z.; software, Y.Z.; validation, H.-Y.L.; formal analysis, Y.-M.H.; resources, C.W.; data curation, Y.Z. and Y.-M.H.; writing—original draft preparation, Y.Z.; writing—review and editing, C.S. and H.-Y.L.; supervision, C.S. and M.L.; funding acquisition, C.W. and C.S. All authors have read and agreed to the published version of the manuscript.

Funding: This research was funded by the National Natural Science Foundation of China, grant number 52301368; the Heilongjiang Provincial Natural Science Foundation of China, grant number JQ2024E007; and the National Natural Science Fund Joint Fund for Regional Innovation and Development, grant number U25A20376.

Data Availability Statement: All hydrodynamic, vortex flow field, and acoustic noise data generated in this numerical simulation, together with mesh files and case files, are kept on the research group's local server. The raw files of flow field and noise calculation take up massive storage space and cannot be publicly uploaded. Access to groove parameters, turbulence results, noise spectra, and sound pressure data can be obtained from the corresponding author after reasonable application.

Conflicts of Interest: Author Min Liu was employed by the company China Shipbuilding Industry Corporation 719th Research Institute. The remaining authors declare that the research was conducted in the absence of any commercial or financial relationships that could be construed as a potential conflict of interest.

References

1. Zhang, Y.; Han, J.; Huang, B.; Zhang, D.; Wu, D. Excitation force on a pump-jet propeller: The effect of the blade number. *Ocean Eng.* **2023**, *281*, 114727. [CrossRef]
2. Zhao, X.; Shen, X.; Geng, L.; Zhang, D.; Van Esch, B.P.M. Comparative study on the wake dynamics of pump-jet and ducted propeller based on dynamic mode decomposition. *Phys. Fluids* **2023**, *35*, 115135. [CrossRef]
3. Shi, Y.; Pan, G.; Huang, Q.; Du, X. Numerical simulation of cavitation characteristics for pump-jet propeller. In *Journal of Physics: Conference Series*; IOP Publishing: Bristol, UK, 2015; Volume 640, p. 012035.
4. Zheng, S.; Huang, Q.; Zhou, L.; Li, H.; He, X.; Li, X. Effects of propeller boss cap fins on hydrodynamics and flow noise of a pump-jet propulsor. *Phys. Fluids* **2024**, *36*, 095104. [CrossRef]
5. Wen, H.; Zhao, W.; Mao, Y.; Zeng, J.; Yu, H.; Zheng, J. Numerical investigation of noise reduction of a pump-jet propulsor using porous metal. *Ocean Eng.* **2024**, *314*, 119736. [CrossRef]
6. Sang, J.A.; Kwon, O.J. Numerical investigation of cavitating flows for marine propulsors using an unstructured mesh technique. *Int. J. Heat Fluid Flow* **2013**, *43*, 259–267. [CrossRef]
7. Ahn, S.J.; Kwon, O.J. Numerical investigation of a pump-jet with ring rotor using an unstructured mesh technique. *J. Mech. Sci. Technol.* **2015**, *29*, 2897–2904. [CrossRef]
8. Ye, J.M.; Sun, D.P.; Zou, X.Y.; Wu, Y.R.; Xi, P. Tip flow control performance and mechanism of axial slots in a pumpjet propulsor. *Ocean Eng.* **2022**, *266*, 112950. [CrossRef]
9. Xiang, Y.; Wang, W. Hydrodynamic performance evaluation of pump-jet propulsion based on the toroidal propeller. *Ocean Eng.* **2024**, *311*, 118932. [CrossRef]
10. Suryanarayana, C.; Satyanarayana, B.; Ramji, K. Experimental evaluation of pumpjet propulsor for an axi-symmetric body in wind tunnel. *Int. J. Nav. Archit. Ocean Eng.* **2010**, *2*, 24–33. [CrossRef]
11. Lu, L.; Pan, G.; Sahoo, P.K. CFD prediction and simulation of a pumpjet propulsor. *Int. J. Nav. Archit. Ocean Eng.* **2016**, *8*, 62–71. [CrossRef]
12. Gómez, G.P.; Adalid, J. Improving the Propulsion Efficiency by means of Contracted and Loaded Tip (CLT®) Propellers. In *Proceedings of the SNAME Athens Conference*; SNAME: Athens, Greece, 2012.
13. Gonzalez-Adalid, J.; Sobrino, M.P.; Gomez, A.G.; Gennaro, G.; Gaggero, S.; Viviani, M.; Sanchez-Caja, A. Comparison of different scaling methods for model tests with CLT propellers. In Proceedings of the 11th International Conference on Hydrodynamics [ICHD], Singapore, 19–24 October 2014.
14. Gaggero, S.; Gonzalez-Adalid, J.; Sobrino, M.P. Design and analysis of a new generation of CLT propellers. *Appl. Ocean Res.* **2016**, *59*, 424–450. [CrossRef]
15. Miorini, R.L.; Wu, H.; Katz, J. The internal structure of the tip leakage vortex within the rotor of an axial waterjet pump. *J. Turbomach.* **2012**, *134*, 031018. [CrossRef]
16. Posa, A. The dynamics of the tip vortices shed by a tip-loaded propeller with winglets. *J. Fluid Mech.* **2022**, *951*, A25. [CrossRef]
17. Wang, C.; Li, P.; Han, Y.; Hao, L. The study on the wake of a CLT propeller under different advance coefficients. *Appl. Ocean Res.* **2022**, *118*, 102996. [CrossRef]
18. Wang, C.; Li, P.; Guo, C.; Wang, L.; Sun, S. Numerical research on the instabilities of CLT propeller wake. *Ocean Eng.* **2022**, *243*, 110305. [CrossRef]
19. Gaggero, S.; Ferrando, M. Wake instabilities of tip-loaded propellers: Comparison between CLT and "new generation" CLT configurations. *J. Mar. Sci. Eng.* **2023**, *11*, 112. [CrossRef]
20. Felli, M.; Camussi, R.; Di Felice, F. Mechanisms of evolution of the propeller wake in the transition and far fields. *J. Fluid Mech.* **2011**, *682*, 5–53. [CrossRef]
21. Gaggero, S.; Tani, G.; Viviani, M.; Conti, F. A study on the numerical prediction of propellers cavitating tip vortex. *Ocean Eng.* **2014**, *92*, 137–161. [CrossRef]
22. Felli, M.; Falchi, M. Propeller wake evolution mechanisms in oblique flow conditions. *J. Fluid Mech.* **2018**, *845*, 520–559. [CrossRef]
23. Posa, A.; Broglia, R.; Balaras, E. The wake structure of a propeller operating upstream of a hydrofoil. *J. Fluid Mech.* **2020**, *904*, A12. [CrossRef]
24. Gaggero, S.; Martinelli, M. Design and analysis of pumpjet propulsors using CFD-based optimization. *Ocean Eng.* **2023**, *277*, 114304. [CrossRef]
25. Guo, C.; Yang, C.; Sun, C.; Wang, C.; Yao, H.; Lin, J. Numerical investigation of the scale effects of pump-jet propulsor with a pre-swirl stator. *Phys. Fluids* **2023**, *35*, 027115. [CrossRef]
26. Lü, X.-J.; Zhou, Q.-D.; Fang, B. Hydrodynamic performance of distributed pump-jet propulsion system for underwater vehicle. *J. Hydrodyn.* **2014**, *26*, 523–530. [CrossRef]
27. Qin, D.; Huang, Q.; Shi, Y.; Pan, G.; Shi, Y.; Dong, X. Comparison of hydrodynamic performance and wake vortices of two typical types of pump-jet propulsor. *Ocean Eng.* **2021**, *224*, 108700. [CrossRef]

28. Li, H.; Huang, Q.; Pan, G.; Dong, X. Wake instabilities of a pre-swirl stator pump-jet propulsor. *Phys. Fluids* **2021**, *33*, 085119. [CrossRef]
29. Williams, J.F.; Hawkings, D.L. Sound generation by turbulence and surfaces in arbitrary motion. *Philos. Trans. R. Soc. London. Ser. A Math. Phys. Sci.* **1969**, *264*, 321–342. [CrossRef]
30. *ISO 1683:2015*; Acoustics—Preferred Reference Values for Acoustical and Vibratory Levels. International Organization for Standardization: Geneva, Switzerland, 2015.

Disclaimer/Publisher's Note: The statements, opinions and data contained in all publications are solely those of the individual author(s) and contributor(s) and not of MDPI and/or the editor(s). MDPI and/or the editor(s) disclaim responsibility for any injury to people or property resulting from any ideas, methods, instructions or products referred to in the content.